PERGAMON

International Journal of Solids and Structures 39 (2002) 3777–3796

INTERNATIONAL JOURNAL OF SOLIDS and STRUCTURES

www.elsevier.com/locate/ijsolstr

Full-field measurements of heterogeneous deformation patterns on polymeric foams using digital image correlation

Yu Wang, Alberto M. Cuitiño *

Department of Mechanical and Aerospace Engineering, Rutgers University, Busch Campus, Engineering Building, Rm D103 98, Brett Road, Piscataway, NJ 08854, USA

Received 13 February 2002

Abstract

The ability of a digital image correlation technique to capture the heterogeneous deformation fields appearing during compression of ultra-light open-cell foams is presented in this article. Quantitative characterization of these fields is of importance to understand the mechanical properties of the collapse process and the energy dissipation patterns in this type of materials. The present algorithm is formulated in the context of multi-variable non-linear optimization where a merit function based on a local average of the deformation mapping is minimized implicitly. A parallel implementation utilizing message passing interface for distributed-memory architectures is also discussed. Estimates for optimal size of the correlation window based on measurement accuracy and spatial resolution are provided. This technique is employed to reveal the evolution of the deformation texture on the surface of open-cell polyurethane foam samples of different relative densities. Histograms of the evolution of surface deformation are extracted, showing the transition from unimodal to bimodal and back to unimodal. These results support the interpretation that the collapse of light open-cell foams occurs as a phase transition phenomenon.

Keywords: Compression; Non-linear; Digital image

1. Introduction

Digital image correlation (DIC) is a computer-vision-based, non-contact, full-field surface strain measuring method. This technique provides estimates of the displacement field by correlating a pair of digital images (before and after a deformation increment is applied) using a mathematically well-defined function. DIC is a *local* measuring method since it only correlates pixels on some subset of pixels (correlation window) of the entire image. DIC is also a *fuzzy* measuring technique since it averages the displacement field over the correlation window.

* Corresponding author. Fax: +1-732-445-3124.
E-mail address: cuitino@jove.rutgers.edu (A.M. Cuitiño).

0020-7683/02/$ - see front matter
PII: S0020-7683(02)00176-2

DIC is a versatile technique which offers adjustable spatial resolution, and thus, it provides measuring capabilities at various length scales. The resolution of the measurements is determined by both the magnification of the acquisition system (optical lenses, scanning electron microscope (SEM), scanning tunneling microscope (STM), atomic force microscope, etc.) and the characteristics of the image sensing elements (pixel pitch of charge-coupled device, resolution of photographic film, inchworm's steplength, etc.)

The versatility of this technique is clear from the wide range of applications including velocity-field measurement of seeded fluid (He et al., 1984), in situ sintering shrinkage measurement of powder compaction (Mizuno et al., 1995), characterization of soil surface layer cracking (Cardenas-Garcia et al., 1998), detection of plastic deformation patterns in aluminum alloy (Tong, 1997), deformation fields around crack tip (Chao et al., 1998), reliability study of microelectronic packages (Lu, 1998), and compression strain measurement of polyurethane foam plastics materials (Zhang et al., 1999) and aluminum alloy foams (Bart-Smith et al., 1998; Bastawros et al., 2000) among many others. Recently, DIC has been used in conjunction with advanced instrumentation systems such as SEM and STM for quantitative material characterization (Yongqi et al., 1996; Lockwood and Reynolds, 1999; Vendroux and Knauss, 1998) and with high-speed photography (Cranz-Schardin camera) for dynamic fracture studies (Chao et al., 1998). Although in many cases the natural texture of the surface provides enough information (speckles) to perform the correlation, artificial speckles are also commonly used to enhance the accuracy of the measurements, for example by imprinting a dot map or markers using a SEM electron beam (Yongqi et al., 1996) or a photo-lithography process (Wissuchek et al., 1996).

DIC was first proposed in the early 80s as an automated approach for the computation of surface strains and displacements (Peters and Ranson, 1982). It was later formulated to study 2D solid mechanics problems, which required a search for six parameters: two rigid displacements, U, V, and four spatial gradients $U_{,x}$, $U_{,y}$, $V_{,x}$, $V_{,y}$ (Chu et al., 1985). This search in this six-dimensional space was conducted by resorting to a two-parameter search approach, which for highly non-linear problems, may render local minima instead of the global minimum. Search efficiency can be improved, however, by introducing a iterative scheme based on a Newton–Raphson approach (Bruck et al., 1989). Although Newton–Raphson methods tend to significantly reduce the computational effort, they also require good estimates of the initial values. In the present formulation, we adopt a Newton–Raphson approach augmented with a derivative-independent iterative scheme, performed on a coarse grid, to estimate the initial values. This combined methodology, which can be inscribed as a multi-grid approach, adds robustness to the search. This approach is also suitable to conduct searches in higher dimensional spaces. Such searches are required when the assumption of uniform deformation within the correlation window is no longer valid. In those cases, six more parameters are added, namely $U_{,xx}$, $U_{,xy}$, $U_{,yy}$, $V_{,xx}$, $V_{,xy}$, $V_{,yy}$ including an additional one to account for the gray-scale value offset due to a change in lighting conditions (Lu and Cary, 2000). The 3D version of DIC, Digital Voulme Correlation (Bay et al., 1999), represents its further application. Therefore, it is worth formulating in the more general 3D form in this paper.

In this paper we show the suitability of the DIC to capture the heterogeneous deformation pattern that appears in low density polymeric foams under compressive loads. In the next section, we describe the correlation procedure which is formulated as a non-linear optimization problem, including a multi-resolution search which improves the Newton–Raphson iterative procedure. In Section 3, we present a series of examples on polyurethane foams of different densities subjected to uniaxial compression. In both cases, the evolution of spatial distribution of the deformation field is recorded and histograms are constructed based on the measurements. These histograms show that in the case of light foams, which exhibit a plateau in the stress–strain curve, there is a transition from a unimodal distribution of the deformation to a bimodal and back to a unimodal. For heavier foams, where no plateau is present, only a unimodal distribution is observed indicating a nearly homogeneous deformation field across the entire sample. These results are in close agreement with a recent theoretical proposition that deformation occurs as a phase transition process (Gioia et al., 2001).

2. Formulation of digital image correlation

We formulate the DIC procedure within the framework of the optimization theory for multi-variable problems. The present algorithm is developed in the context of a multi-grid approach, involving two main steps: coarse and fine search. The coarse search provides an estimate of the displacement field, which is later used as an initial condition for a fine search using a Newton–Raphson procedure. In the coarse search the gradient terms are kept constant and only the displacement field is allowed to change. In addition, the displacement increments are constrained to change by an integer number of spacing between pixels. The search procedure, which does not require the evaluation of any field derivatives, seeks to find the best correlation between a window in the reference image and a window in the deformed one. The degree of the correlation is measured by the values adopted by the merit or correlation function, which is described in Section 2.1. In the coarse search, we first select a window in the reference image and the twin one in the deformed state. Then, we shift the second window by one pixel along 8 different paths ($\theta = n\pi/4$ with $n = 1, 8$) while monitoring the value of the correlation function. The direction which improves the correlation is accepted and the window is permanently shifted in that direction. This procedure is performed until no further improvement is achieved. By composing the shifting path, an estimate of the displacement field is obtained. These values are adopted by the fine search scheme as initial conditions. The fine search, which is described in detail in Section 2.2, then provides resolution up to a desired fraction of the distance between pixels. Both coarse and fine searches are performed at every correlation window but the algorithms are local and a parallel approach by domain decomposition can be effectively resorted to involving no communication among processors. Finally, the need for the coarse search may be alleviated by introducing the continuity condition among different correlation windows. This scheme is described briefly in Section 2.3.

2.1. Correlation function

DIC is a technique based on the analysis of a pair of digital images of a prescribed region V taken before and after a deformation increment is applied. The information of these images is contained in the structure or distribution of the gray values. We denote with $F(\mathbf{X})$ the gray distribution for the undeformed image and with $f(\mathbf{x})$ the gray distribution for the deformed one. In addition, $\mathbf{X}$ and $\mathbf{x}$ are the local coordinate systems in the undeformed and deformed images respectively. A central assumption pertaining DIC is that the gray distribution is preserved by the application of deformation field, realizing only a translation, rotation, stretch and/or distortion according to the applied field. In other words, it is assumed that there is a one-to-one correspondence between the gray distribution on the pictures corresponding to the undeformed and deformed states. Such a function is described by a deformation mapping $\mathbf{x} = \mathbf{x}_0(\mathbf{X})$ such that $F(\mathbf{X}) = f[\mathbf{x}_0(\mathbf{X})]$. The correlation function, χ^2, is then naturally obtained as a distance measure between $F(\mathbf{X})$ and $f(\mathbf{x})$. More precisely, it is defined as a least-square cross-correlation coefficient, C, given by

$$\chi^2 = C[\mathbf{x}(\mathbf{X})] = \frac{\int_V \left\{ \frac{f[\mathbf{x}(\mathbf{X})] - F(\mathbf{X})}{\sigma(\mathbf{X})} \right\}^2 \mathrm{d}^3X}{\int_V F^2(\mathbf{X}) \mathrm{d}^3X}, \tag{1}$$

where the integrals are performed over the material volume V, $\sigma(\mathbf{X})$ is the standard deviation at each point due to measurement and $\mathbf{x}(\mathbf{X})$ is a given deformation mapping. The optimality condition is achieved for $\mathbf{x}(\mathbf{X}) = \mathbf{x}_0(\mathbf{X})$ which renders $\chi^2 = 0$. Then $\mathbf{x}_0(\mathbf{X})$ is called the *optimizer*.

The above expression can be further simplified since $\sigma(\mathbf{X})$ are deviations introduced by the measurement and they are independent of $\mathbf{X}$.

Furthermore, the denominator for a specified volume V remains constant. Both terms can then be safely removed from the Eq. (1) without loss of generality. The expression for the merit function is reduced to

$$\chi^2 = C[\mathbf{x}(\mathbf{X})] = \int_V \{f[\mathbf{x}(\mathbf{X})] - F(\mathbf{X})\}^2 \mathrm{d}^3X \tag{2}$$

which is a functional of the mapping function $\mathbf{x}(\mathbf{X})$. In order to efficiently obtain an optimizer of this correlation function, a derivative-based iterative procedure is adopted, which requires the computation of the first (Jacobian) and second (Hessian) order derivatives, which are provided in Section 2.2 for a given interpolation scheme.

2.2. Minimization of the correlation function—fine search

A simple scheme for interpolating the displacement field inside a given correlation window (a cube or a rectangular parallelepiped in a general 3D case) can be obtained by utilizing the information at its central point. If we assume that the *local* deformation field is homogeneous, only a first-order (linear) interpolation is required to reconstruct the displacement field within that region.

Consider then a material point in given correlation window $\mathbf{X}_\mathrm{p} = \mathbf{X}_\mathrm{c} + \Delta\mathbf{X}_\mathrm{p}$ (see Fig. 1), where the subscript "c" indicates the central point and "p" represents its neighboring points, the corresponding point in the deformed configuration is given by

$$\mathbf{x}(\mathbf{X}_\mathrm{p}) = \mathbf{X}_\mathrm{c} + \mathbf{u}(\mathbf{X}_\mathrm{c}) + \left[\frac{\partial \mathbf{u}}{\partial \mathbf{X}}\right]_{\mathbf{X}_\mathrm{c}} \Delta\mathbf{X}_\mathrm{p}, \tag{3}$$

with

$$\mathbf{u}(\mathbf{X}_\mathrm{c}) = \begin{bmatrix} u_\mathrm{c} \\ v_\mathrm{c} \\ w_\mathrm{c} \end{bmatrix} \tag{4}$$

and

$$\left[\frac{\partial \mathbf{u}}{\partial \mathbf{X}}\right]_{\mathbf{X}_\mathrm{c}} = \begin{bmatrix} u_{\mathrm{c},x} & u_{\mathrm{c},y} & u_{\mathrm{c},z} \\ v_{\mathrm{c},x} & v_{\mathrm{c},y} & v_{\mathrm{c},z} \\ w_{\mathrm{c},x} & w_{\mathrm{c},y} & w_{\mathrm{c},z} \end{bmatrix}. \tag{5}$$

The local mapping function $\mathbf{x}(\mathbf{X})$ is then

$$\mathbf{x}(\mathbf{X}) = \mathbf{x}(\mathbf{X}_\mathrm{c}, \Delta\mathbf{X}, \mathbf{p}) \tag{6}$$

where the vector $\mathbf{p}$ has twelve components,

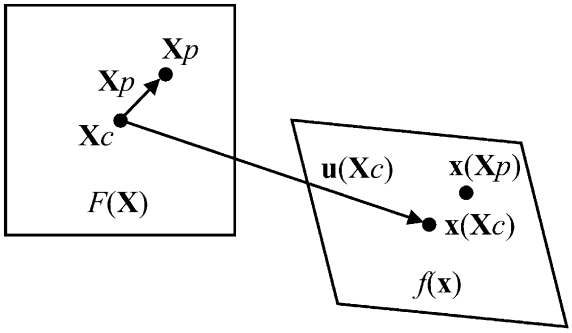

Fig. 1. A correlation window and the central point.

$$\mathbf{p} = [\, u_c \quad v_c \quad w_c \quad u_{c,x} \quad u_{c,y} \quad u_{c,z} \quad v_{c,x} \quad v_{c,y} \quad v_{c,z} \quad w_{c,x} \quad w_{c,y} \quad w_{c,z} \,]^T. \tag{7}$$

By using Eqs. (6) and (7), the correlation function in Eq. (2) degenerates into a function of the vector $\mathbf{p}$,

$$\chi^2 = C(\mathbf{p}) = \int_{V_{\text{window}}} \{f[\mathbf{x}(\mathbf{X}_c, \Delta\mathbf{X}, \mathbf{p})] - F(\mathbf{X}_c, \Delta\mathbf{X})\}^2 \mathrm{d}^3\Delta X. \tag{8}$$

The first derivative, the Jacobian $\mathbf{J}$, may be evaluated as

$$\mathbf{J} = \frac{\partial\chi^2}{\partial\mathbf{p}} = \frac{\partial C(\mathbf{p})}{\partial\mathbf{p}} = \int_{V_{\text{window}}} 2\{f[\mathbf{x}(\mathbf{X}_c, \Delta\mathbf{X}, \mathbf{p})] - F(\mathbf{X}_c, \Delta\mathbf{X})\} \frac{\partial f[\mathbf{x}(\mathbf{X}_c, \Delta\mathbf{X}, \mathbf{p})]}{\partial\mathbf{p}} \mathrm{d}^3\Delta X, \tag{9}$$

where the derivative $\partial f[\mathbf{x}(\mathbf{X}_c, \Delta\mathbf{X}, \mathbf{p})]/\partial\mathbf{p}$ can be computed using chain rule

$$\frac{\partial f[\mathbf{x}(\mathbf{X}_c, \Delta\mathbf{X}, \mathbf{p})]}{\partial\mathbf{p}} = \frac{\partial f(\mathbf{x})}{\partial\mathbf{x}} \frac{\partial\mathbf{x}(\mathbf{X}_c, \Delta\mathbf{X}, \mathbf{p})}{\partial\mathbf{p}}. \tag{10}$$

The second term in the above expression can be evaluated explicitly by virtue of Eqs. (3)–(5)

$$\frac{\partial\mathbf{x}(\mathbf{X}_c, \Delta\mathbf{X}, \mathbf{p})}{\partial\mathbf{p}} = \begin{bmatrix} 1 & 0 & 0 & \Delta X & \Delta Y & \Delta Z & 0 & 0 & 0 & 0 & 0 & 0 \\ 0 & 1 & 0 & 0 & 0 & 0 & \Delta X & \Delta Y & \Delta Z & 0 & 0 & 0 \\ 0 & 0 & 1 & 0 & 0 & 0 & 0 & 0 & 0 & \Delta X & \Delta Y & \Delta Z \end{bmatrix}, \tag{11}$$

while the first term is numerically computed from the distribution $f(\mathbf{x})$, which depends on the particular selection of interpolation functions, such as bilinear or bicubic.

The second derivative, the Hessian $\mathbf{H}$, of the correlation function χ^2 is given by

$$\begin{aligned} \mathbf{H} = \frac{\partial^2\chi^2}{\partial\mathbf{p}^2} = \frac{\partial^2 C(\mathbf{p})}{\partial\mathbf{p}^2} &= \int_{V_{\text{window}}} 2 \frac{\partial f[\mathbf{x}(\mathbf{X}_c, \Delta\mathbf{X}, \mathbf{p})]}{\partial\mathbf{p}} \otimes \frac{\partial f[\mathbf{x}(\mathbf{X}_c, \Delta\mathbf{X}, \mathbf{p})]}{\partial\mathbf{p}} \mathrm{d}^3\Delta X \\ &+ \int_{V_{\text{window}}} 2\{f[\mathbf{x}(\mathbf{X}_c, \Delta\mathbf{X}, \mathbf{p})] - F(\mathbf{X}_c, \Delta\mathbf{X})\} \frac{\partial^2 f[\mathbf{x}(\mathbf{X}_c, \Delta\mathbf{X}, \mathbf{p})]}{\partial\mathbf{p}^2} \mathrm{d}^3\Delta X \end{aligned} \tag{12}$$

The second integral of Eq. (12) can be neglected due to the following practical consideration (Press et al., 1992): The term $f[\mathbf{x}(\mathbf{X}_c, \Delta\mathbf{X}, \mathbf{p})] - F(\mathbf{X}_c, \Delta\mathbf{X})$ in the vicinity of solution attains random values of either sign on the account of measurement errors. Therefore, the second integral containing the second derivatives tends to vanish upon integration. The Hessian matrix is then written as

$$\mathbf{H} = \frac{\partial^2\chi^2}{\partial\mathbf{p}^2} = \frac{\partial^2 C(\mathbf{p})}{\partial\mathbf{p}^2} = \int_{V_{\text{window}}} 2 \frac{\partial f[\mathbf{x}(\mathbf{X}_c, \Delta\mathbf{X}, \mathbf{p})]}{\partial\mathbf{p}} \otimes \frac{\partial f[\mathbf{x}(\mathbf{X}_c, \Delta\mathbf{X}, \mathbf{p})]}{\partial\mathbf{p}} \mathrm{d}^3\Delta X \tag{13}$$

where only the first order derivatives are involved.

With the assistance of the Jacobian and Hessian, the local mapping function $\mathbf{x}(\mathbf{X})$ can be iteratively approximated by minimizing the correlation function χ^2 by recursively applying

$$\mathbf{p}_{n+1} = \mathbf{p}_n - \mathbf{H}_n^{-1}\mathbf{J}_n \tag{14}$$

where n indicates the iteration step.

This iteration scheme is *local* and only the values at the central point of correlation window are considered. The local environment of that point defines a spatial pattern (speckle in 2D case), which is recognized before and after deformation. An actual speckle pattern obtained on the surfaces of an original and deformed polymeric foam specimen is shown in Fig. 2. The measurement of full-field is then obtained by resorting to this procedure for each correlation window. Since this algorithm does not require communication of information from neighboring correlation windows, it is ideally suited for massive parallelization.

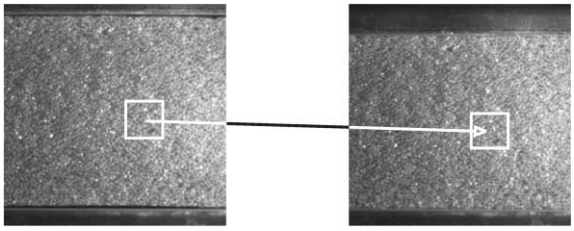

Fig. 2. Speckles are the information carriers.

In fact, the correlations presented in Section 3 have been obtained by an in-house implementation using message passing interface (MPI) running on a computer cluster with a distributed memory architecture.

Now we turn our attention to the evaluation of the function $f(\mathbf{x})$ and its derivative $\partial f(\mathbf{x})/\partial \mathbf{x}$, which are required in the Newton–Raphson search. Although the function $f(\mathbf{x})$ is known at every pixel, we need to estimate its value (and derivatives) in between pixels, and for that purpose we introduce an interpolation scheme. It should be noted that this interpolation is independent of the deformation mapping $\mathbf{x}(\mathbf{X})$ and it is only computed once for the image in the deformed configuration. The order of the interpolation is usually selected based on computational complexity and accuracy.

In the present work, we consider two different interpolation schemes: bi-linear and bi-cubic. In the first case, only the gray values at the four pixels delimiting the interpolation domain are needed, while for the second case, the additional 12 pixels enclosing the interpolation domain, are used (Fig. 3). The implication of theses different interpolation schemes in the context of foams mechanics are described in Section 3.

2.3. Displacement continuity

The computational burden of the coarse search can be greatly reduced by exploiting the condition that the displacements are continuous across correlation windows, which is a frequent condition apart from

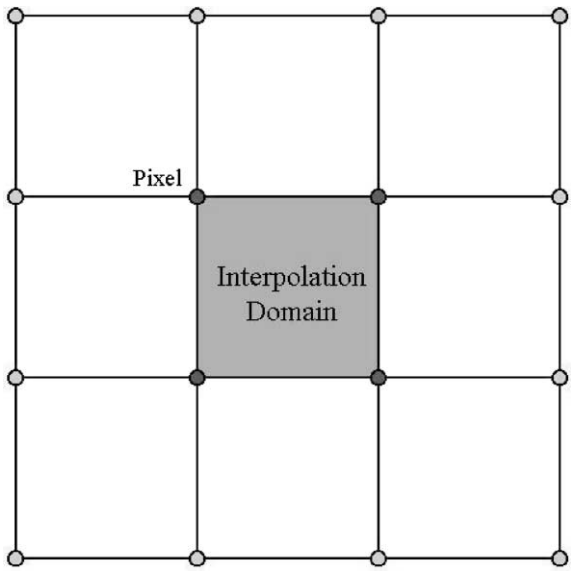

Fig. 3. Schematic of the interpolation domain. Pixels shaded in dark gray are needed for bilinear interpolation, pixels shaded in light gray are also required for the bi-cubic interpolation.

problems involving fracture. This approach allows us to perform this costly coarse search in only one window instead of in every one. The overall scheme proceeds as follows: a combined search is performed in a given correlation window followed by the fine search. This step provides estimates of the displacement field including its spatial variation. Then, by assuming continuity, we extrapolate the displacement field to the neighboring windows to estimate the value at the center point. In this manner, the coarse search is only performed once but the procedure is now sequential. A given window, except for the first one, requires the completion of the fine search in a neighboring window before initiating its own.

While the initial algorithm (coarse search everywhere) is in principle highly efficient for parallel computing regardless of the number of pixels per processor, the second one remains well suited for parallelization when a large number of pixels is associated to each processor, which is usually the case in most applications and certainly for extensions to 3D problems. For these cases, this procedure is performed in every domain, resulting in only one coarse search per domain.

3. Digital image correlation on foam mechanics

In this section we describe specific implementation issues and results pertaining to the application of the DIC technique to study the behavior of polymeric foam subjected to compressive loading. We first verify the accuracy of the technique to capture an applied displacement field, which is presented in some detail in Section 3.1. In that section we also describe the experimental setup and the implication of the different interpolation schemes (bi-linear and bi-cubic) on the optimal selection of the correlation window size. One interesting observation is that the natural porous texture of the specimen surface, under proper (oblique incidence) lighting condition and proper imaging magnification, produces high-quality speckles (as shown in Fig. 2), carrying sufficient information to perform the correlation.

3.1. Verification of digital image correlation for polymeric foams

We study the accuracy of the DIC by imposing a rigid body translation and rotation to a foam sample, according to the experimental setup shown in Fig. 4. We select these tests for verification since the exact value at every position is precisely known and it can be directly compared against the experimental

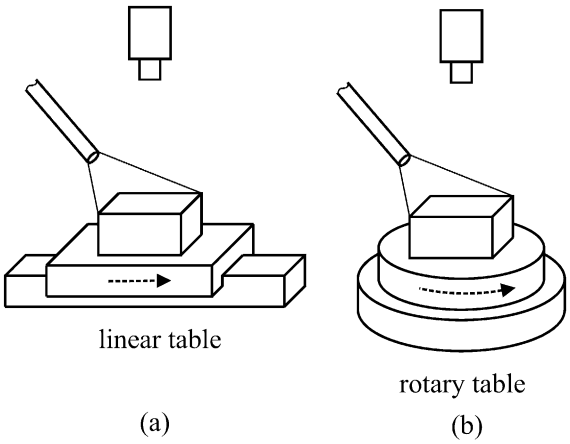

Fig. 4. The experimental setup for a validation of DIC's application to foam mechanics. (a) Rigid body translation using a linear table. (b) Rigid body rotation using a rotary table.

measurements. For other tests, where a deformation field is imposed (e.g. uniform deformation), only the average value is known due to inhomogeneities at local level induced by the heterogeneous nature of the microstructure.

For the rigid body translation test, we utilize a motorized linear table (Parker 404XR linear positioning table with ZETA4 micro-stepping system and Renishaw RGH22 linear encoder system) with an accuracy of 1 μm (Fig. 4a), while for the rotation test, we use a manual rotary table (Newport UTR80 precision manual rotary stage) with an accuracy of 1 arcmin (Fig. 4b). A digital CCD camera (PULNiX TM-9701 progressive scan monochrome CCD camera) is used to obtain high-quality digital images, where the electromagnetic noise during video signal transmission is effectively reduced to negligible level. A telecentric video lens (Computar 55 mm telecentric lens with F# 2.8-32C) is used as the optical imaging system for CCD camera. A telecentric lens is chosen because it provides a constant magnification over a range of working distances virtually eliminating viewing angle error. Thus, a telecentric lens is ideal in machine vision applications requiring accurate measurement of 3D surfaces with slightly height variations. By eliminating the perspective distortion and magnification error inherent in conventional lenses, a telecentric lens yields dimensionally accurate images that are easily interpreted by the software. The lighting is provided using a fiber optic light source (Mille Luce M1000 fiber optic illuminator with dual branch light guide).

We first conduct a parametric study of the effect of the correlation window size and the interpolation scheme. For that purpose, we apply a rigid body displacement acquiring a series of images along the path. We then perform the correlation for various correlation window sizes and for the bi-linear and bi-cubic interpolation. A statistical analysis of the computed values, mean displacement and its standard variation, for an area of 32×32 is presented in Fig. 5. Two main conclusions can be obtained from the Fig. 5a. The first is that the bi-cubic interpolation converges to the exact imposed displacement, while the bi-linear does not. The second is that a relatively small correlation window of approximately 15×15 pixels is sufficient for recovering accurate values. From Fig. 6b, we also conclude that the bi-cubic interpolation provides lower and consistent standard deviation of about 0.04 pixels.

The accuracy of the measurement for the translation and rotation is shown in Fig. 6, where a correlation window of 15×15 pixels and bi-cubic interpolation were used. The motion was applied in several and equal step, acquiring images at every step. The correlation was then performed between sequential pairs of images. The total translation and rotation was obtained by adding the incremental field obtained for each step. These values are plotted in Fig. 6. It is clear from the plots that the equal increments in the applied field translate into equal increments of measured values as attested by the linear relation. For the case of translation shown in Fig. 6a, the correlation is excellent and the imposed displacement is recovered. For the case of rotation shown in Fig. 6b, an error of about 5% is recorded. The source of this systematic error is

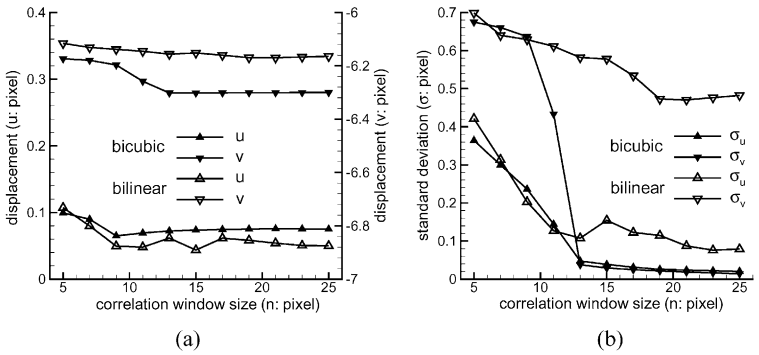

Fig. 5. A statistical assessment of DIC measurement with respect to correlation window size and interpolation procedures. (a) Mean. (b) Standard deviation.

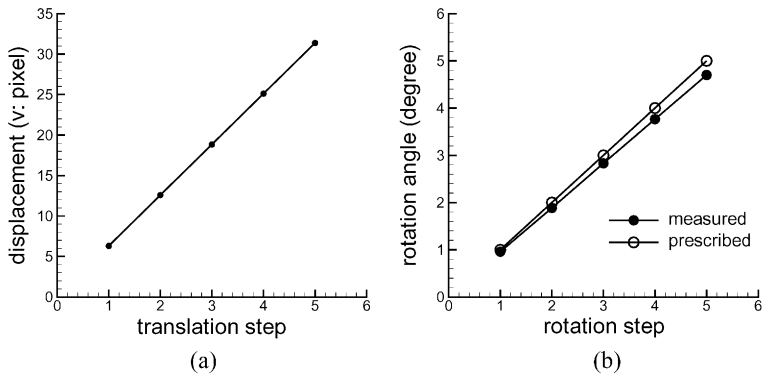

Fig. 6. DIC measurement of rigid body translation and rotation, respectively, with optimal parameters, 15×15 correlation window and bi-cubic interpolation. (a) Rigid body translation. (b) Rigid body rotation.

associated to the non-square sensing cell of the CCD, which can be compensated algorithmically by introducing the CCD pixel ratio into the formulation. For the present application, however, where the existence of highly heterogeneous fields are sought, this error is deemed acceptable. This verification clearly demonstrates that the present formulation and implementation of the DIC can be employed to conduct studies in polymeric foams.

Before proceeding to analyze the deformation patterns on compressed foams, we note that in order to follow the large deformation and heterogeneous fields observed in these studies, the deformation increments should be kept relatively small. There are two reasons for such an imposition. First, the estimates of the initial values for the fine search are obtained by extrapolating the current spatial gradient, which has large variation during the loading process. Second, the local gray distribution (speckle) needs to be traced. Thus, the deformation is imposed by many sequential increments and the total fields are obtained by accumulation. We also note that the error in the vicinity of some microstructural defects, such as voids, may be substantially larger than the average due to the lack of information in that region. An example of such a case is shown in Fig. 7 where a region of about 5 pixels (circled) appears completely black or white. It is observed that a larger correlation window tends to reduce the error in those regions.

3.2. Application: heterogeneous deformation under uniaxial compression

3.2.1. Theoretical background

In a recent theoretical study (Gioia et al., 2001), it has been proposed that the heterogeneous deformation pattern observed in low-density polymeric foams may be interpreted as phase transition process, where the imposed average deformation in the immiscibility gap is realized by a mixture of two characteristic deformations. According to this theory, the increment in the deformation is obtained by a change in the composition of the mixture rather than by increasing the deformation in each "phase". The underlying physics governing this transformation can be found in the non-convex landscape exhibited by the deformation energy during uniaxial compression.

With the purpose of illustrating and identifying the main factors shaping the energy landscape, we present a simple expression for the energy density. It is obtained by limiting the analysis to a linear elastic open-cell foam with diamond-like structure which is subjected to uniaxial compressive deformation along the vertical direction (see Fig. 8). Additionally, we impose a constrained kinematics, where the bending deformation is concentrated at the joints. A more general expression considering non-linear materials,

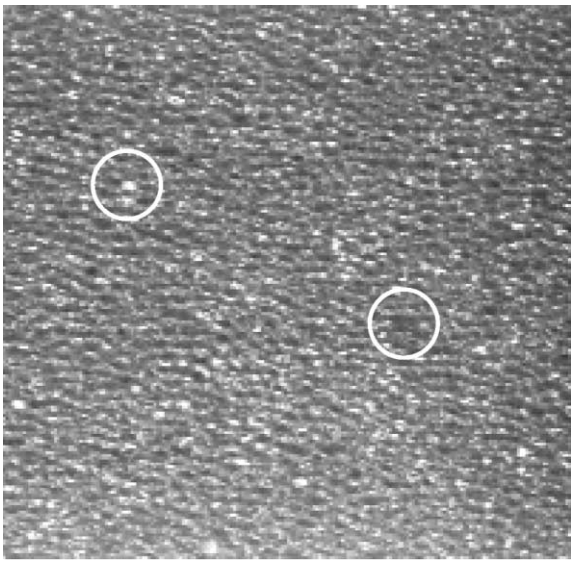

Fig. 7. Defects in the digital images are the regions circled in white. There is a weak speckle effect in these regions, and a reliable correlation cannot be performed.

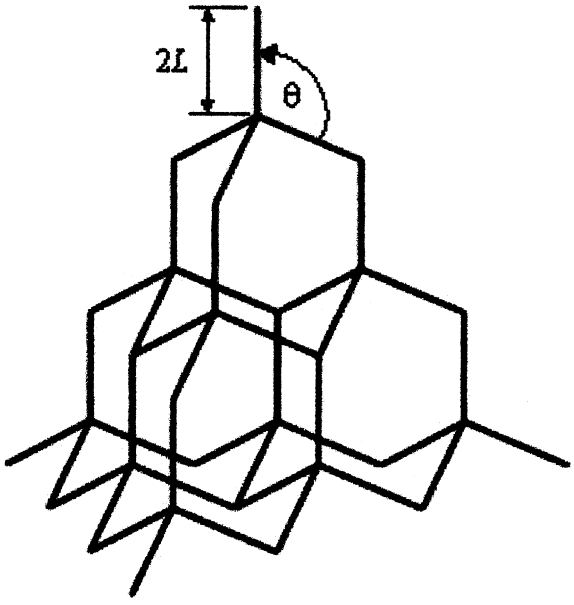

Fig. 8. Schematic of the diamond-like structure.

distorted structures and a general 3D deformation is presented in Wang and Cuitiño (2000). Also, an expression for a linear elastic material under uniaxial deformation utilizing von Kármán theory is derived in Gioia et al. (2001).

Following Wang and Cuitiño (2000), the deformation energy density, w, per unit volume of solid material, V_s, normalized by the Young Modulus of the solid material, E_s, can be expressed as the sum of the contributions from the stretching energy

$$w_{\mathcal{N}} = \frac{3}{8}\left(1 - \frac{\sin\theta_0}{\sin\theta}\right)^2 \left(1 + 3\cos^2\theta\right) + \frac{3\sqrt{3}}{\pi}(\theta - \theta_0)(\sin\theta - \sin\theta_0)\cos\theta\rho + \frac{6}{\pi^2}(\theta - \theta_0)^2 \sin^2\theta\rho^2 \quad (15)$$

and bending energy

$$w_{\mathcal{M}} = \frac{\sqrt{3}}{2\pi}(\theta - \theta_0)^2\rho, \quad (16)$$

where θ is the angle between the inclined member and the vertical axis, $\theta_0 = \arccos 1/3$ is the initial angle and ρ is the relative density of the foam given by

$$\rho = \frac{V_s}{V} = \frac{3\sqrt{3}}{4^2}\pi\left(\frac{r}{L}\right)^2, \quad (17)$$

where V is the volume of a unit cell, V_s is the volume occupied by the solid within the unit cell, $2L$ is the length of each member and r is the radius of the corresponding cross section. Additionally, the compressive strain of the foam ϵ can be related to θ and ρ by

$$\epsilon = 1 - \left(1 - \cos\theta + 4\frac{\sin\theta_0}{\tan\theta} - \frac{4\sqrt{3}}{\pi}\sin\theta(\theta - \theta_0)\rho\right)/(1 + \cos\theta_0). \quad (18)$$

The total deformation energy density is then a function of compressive strain and density,

$$w[\epsilon, \rho] = w_{\mathcal{N}}[\theta(\epsilon, \rho), \rho] + w_{\mathcal{M}}[\theta(\epsilon, \rho), \rho] \quad (19)$$

and the compressive stress (normalized by $\rho\, E_s$) follows naturally as,

$$\Sigma[\epsilon, \rho] = \frac{\mathrm{d}w[\epsilon, \rho]}{\mathrm{d}\epsilon}, \quad (20)$$

where both strain and the stress are assumed as positive in the compressive regime.

In Fig. 9a and b, w and Σ are plotted against ϵ and ρ. It is clear from the figure that there are non-convex regions in the energy landscape, in fact, non-convexity is observed for low values of ρ, while for higher values the energy is convex. The stress, consequently, exhibits a drop for low ρ and hardening for higher ρ.

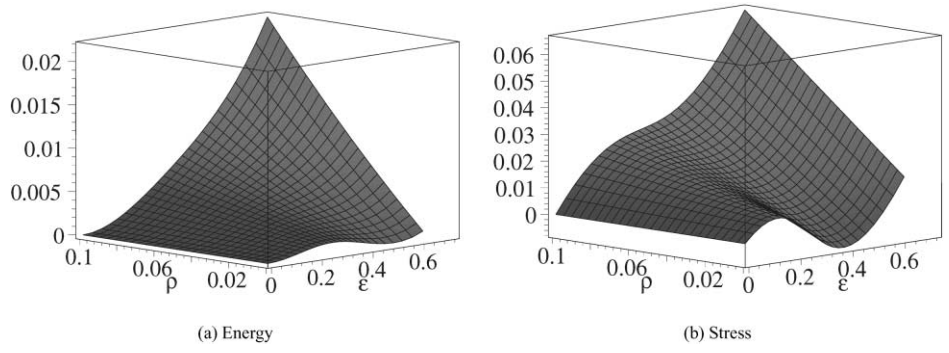

Fig. 9. Normalized energy density and corresponding stress as a function of the applied compressive strain ϵ for different values of the relative density ρ.

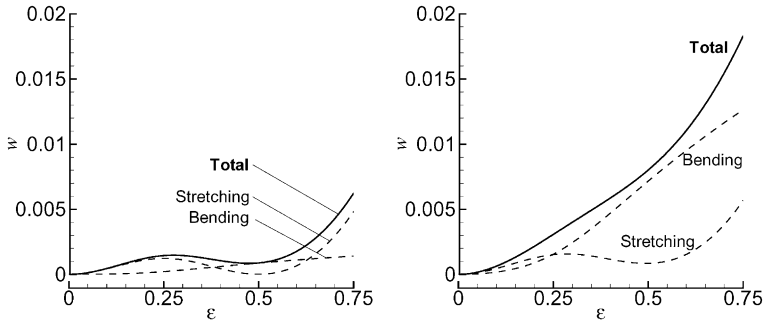

Fig. 10. Normalized deformation energy density as a function of compressive strain ϵ for two different foam densities. The plots show the contribution of the stretching and bending energy to the total energy.

This simple model provides a clear physical picture of the origin of the non-convex/convex regions and the role of the relative density. In Fig. 10, the stretching, bending and the total energies are plotted for two representative (low/high) values of the foam density. It can be observed that the stretching energy is always non-convex regardless of the foam density. This is due to the relaxation mechanism associated with the *snap-back* buckling of the structure when $\theta = \pi/2$. On the other hand, the bending energy is nearly convex for all values of the density. The resulting behavior is then defined by the relative contributions of the stretching and bending to the total energy, and these contributions are strongly dependent on the foam density. For low density the bending has a negligible effect, in fact,

$$w \to w_{\mathscr{N}} \to \frac{3}{8}\left(1 - \frac{\sin\theta_0}{\sin\theta}\right)^2 \left(1 + 3\cos^2\theta\right) \quad \text{and} \quad w_{\mathscr{M}} \to 0 \quad \text{as} \quad \rho \to 0 \tag{21}$$

resulting in a non-convex behavior. For higher densities, bending dominates and the total energy becomes convex. A critical foam density ρ_c can be defined as the value which separates the non-convex and convex regions. In the context of the present discussion, low-density foams ($\rho < \rho_c$) exhibit a non-convex energy structure while high-density foams ($\rho > \rho_c$) show a convex one.

We turn our attention to the implication of the non-convexity on the effective response of the foam. The appearance of such a non-convex region implies that for deformation fields with $\epsilon = \epsilon^*$ where $\epsilon_L < \epsilon^* < \epsilon_H$ (see Fig. 11a), the energy is minimized by a mixture of phases with deformations $\epsilon = \epsilon_L$ and $\epsilon = \epsilon_H$. The volume fraction of phase with $\epsilon = \epsilon_H$ for a given value of ϵ^* can be obtained from the rule of mixtures, i.e.

$$\eta_H(\epsilon^*) = \frac{\epsilon^* - \epsilon_L}{\epsilon_H - \epsilon_L}. \tag{22}$$

The range $\Delta\epsilon = \epsilon_H - \epsilon_L$, which results from combining Euler's Equation and Weierstrass–Erdman corner condition (Bliss, 1961), can be expressed as

$$\Delta w = \mathscr{F}\Delta\epsilon, \tag{23}$$

where $\Delta w = w(\epsilon_H) - w(\epsilon_L)$ and

$$\mathscr{F} = \left.\frac{dw(\epsilon)}{d\epsilon}\right|_{\epsilon_H} = \left.\frac{dw(\epsilon)}{d\epsilon}\right|_{\epsilon_L} = \Sigma(\epsilon_H) = \Sigma(\epsilon_L) \tag{24}$$

as shown in Fig. 11b. Additionally, this condition implies the equality in the areas A_H and A_L.

Thus, within the immiscibility gap, defined by $\Delta\epsilon = \epsilon_H - \epsilon_L$, the energy is minimized by the mixture of two characteristic strains, ϵ_L and ϵ_H. The energy density for the mixture, which is represented by the dash

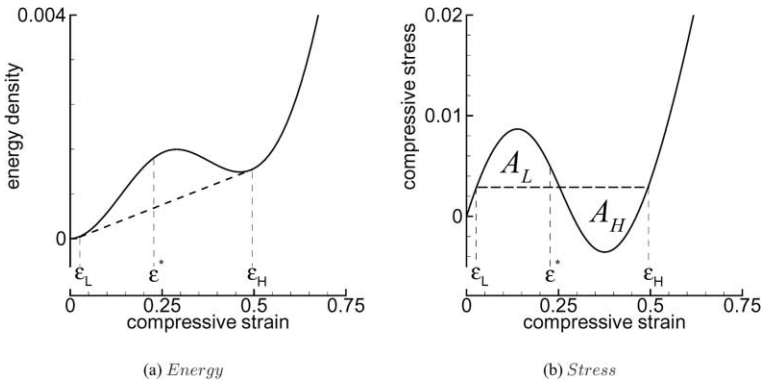

Fig. 11. Normalized deformation energy and normalized stress for uniaxial compression.

line in Fig. 11a, is clearly lower than the energy for an homogeneous state. The corresponding stress, the slope of the energy density plot, results in a constant for $\epsilon_L \leqslant \epsilon \leqslant \epsilon_H$ as indicated by the dash line in Fig. 11b.

In summary, the theory predicts that non-convexity gives rise to a *spatially heterogeneous deformation field* and a *stress plateau* within the immiscibility gap. In the convex regions, however, the deformation remains spatially uniform and the stress is monotonically increasing.

3.2.2. Experimental testing

The spatially heterogeneous deformation can be clearly detected by plotting the evolution of the strain distribution density diagrams (histograms) as a function of the applied average strain. The strain distribution density, $\mathscr{D}(\epsilon)$, is the fraction of total surface with a given strain ϵ. The evolution of these histograms for the ideal case, which amounts to a perfectly homogeneous material with ideal boundary conditions and with a negligible width for the transition region between phases, is shown in Fig. 12. The theory predicts that in the region where the average deformation is in the immiscibility gap, the distribution density shows a bimodal structure (heterogeneous deformation), while outside of the gap a unimodal distribution prevails. Under ideal conditions the distributions are delta "functions", however, if the hypothesis of spatial material homogeneity is relaxed due to irregular cells, defects, etc., the distributions spread around ϵ_L and ϵ_H, as indicated in Fig. 13a. In addition, if we consider that the transition between the regions with the characteristic strains ϵ_L and ϵ_H has a finite width, then non-zero values in the distribution density are observed within that gap as indicated in Fig. 13b. For heavy foams, in contrast, the distribution density remains unimodal irrespective of the value of the applied deformation.

Guided by this theoretical framework, we tested a set of relatively light (21 kg/m^3 or 1.3 PCF [1]) and heavy (72 kg/m^3 or 4.5 PCF) open-cell polyurethane foam samples while recording digital images for *a posteriori* correlation using the DIC formulation described in Section 2. In both cases, the magnification is such that 1 mm on the specimen surface corresponds to eight pixels in the digital image. The average cell size is about 0.5 mm for low-density foam and 0.15 mm for high-density foam. Therefore, a 15×15 window contains roughly 4×4 cells and 13×13 cells for cases of low- and high-density foams, respectively. The specimens were compressed using aluminum platen driven by motorized linear table (as discussed in Section 3.1). Since lubricant will contaminate the foam specimen, there is no special preparation of the interface between the specimen and the compression platen. To reduce the boundary effect due to the friction, we performed DIC in the central part of the specimen where this effect is negligible.

[1] Pounds per cubic foot.

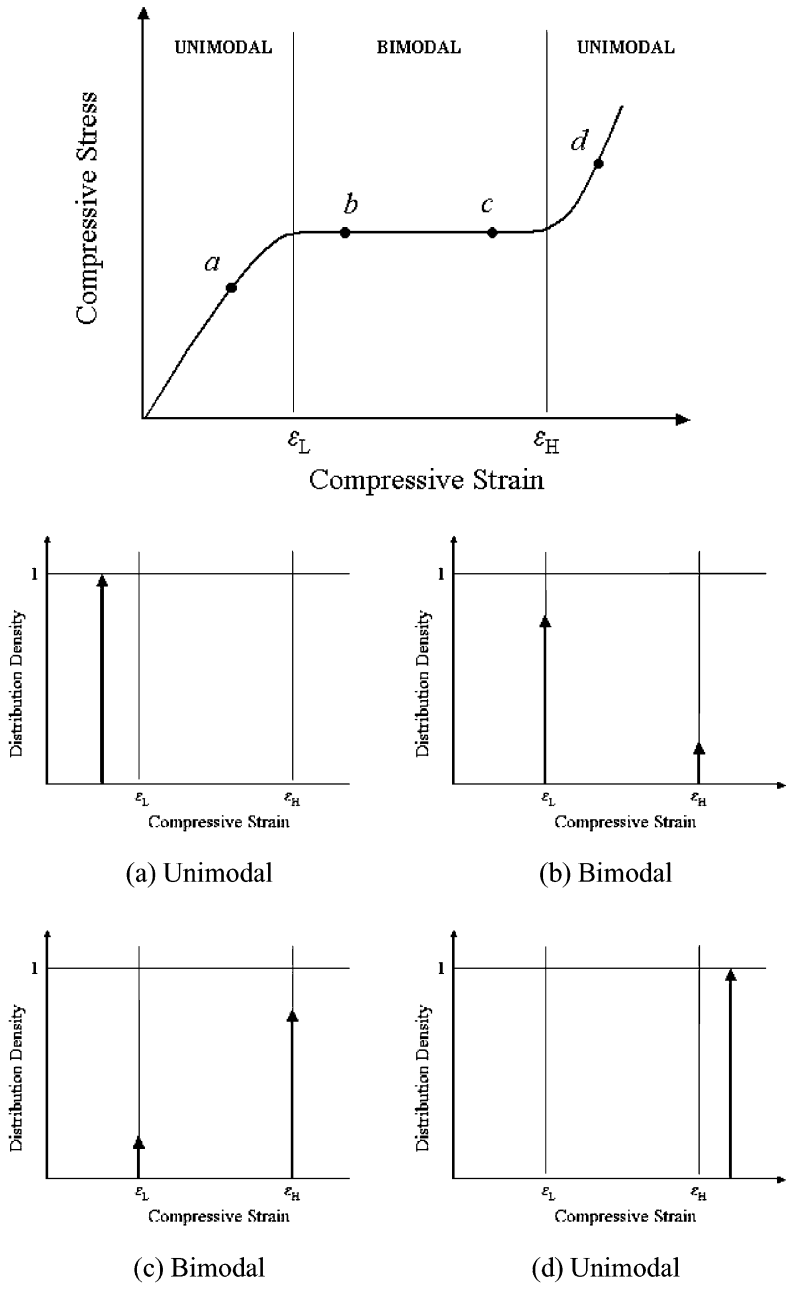

Fig. 12. Schematic of a corollary of the theory proposed in Wang and Cuitiño (2000) and Gioia et al. (2001) for uniaxial compression of foams. The stress–strain curve shows three stages, an initial region of increasing stress, a second regime characterized by a plateau, and finally a third or densification region with increasing stress. During the first and last regime, a unimodal distribution of strain is observed while in the plateau regime, a bimodal one. (a–d) Schematic of the distribution density as a function of the average strain ϵ for the ideal case corresponding to the (a–d) states in the stress–strain curve.

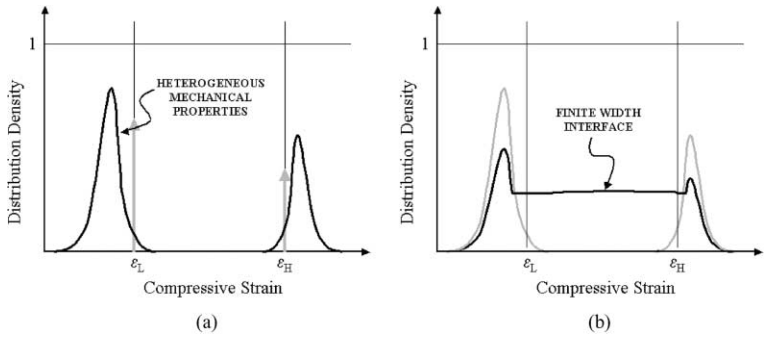

Fig. 13. Schematic of the extension of the theory presented in Wang and Cuitiño (2000) and Gioia et al. (2001) for non-ideal conditions. (a) Effect of inhomogeneity in the material properties or boundary conditions. (b) Additional effect of finite interface width.

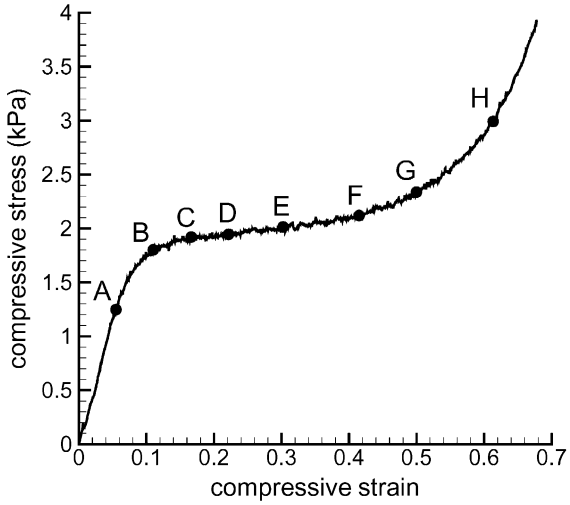

Fig. 14. Stress–strain curve of low density (21 kg/m^3) open-cell polyurethane foam sample under uniaxial compression.

For the low-density case, a cubic specimen ($36 \times 36 \times 36$ mm^3) was compressed at a speed of 0.1 mm/s until an average compressive strain of ~70% was achieved. 23 images of one lateral face of the specimen were taken at equal intervals of loading path. Successive images were correlated, one pair at a time, to compute the displacement field.

In Fig. 14 we show the stress–strain response of the low-density foam. The curve shows the characteristic three-stage response: an initial (nearly) linear regime followed by a stress plateau and a final stage governed by a rapid increase of the stress. This response is consistent with the theory previously described. Fig. 15 shows the contour plots of the displacement field at different values of the average applied strain. These values are marked by the letters A to H in Fig. 14. The heterogeneous nature of the deformation is clearly demonstrated by the different spacing between the contour lines. It can be observed from the figure that the process of localization is governed by nucleation and growth, where a seed (small region with close spacing) is first nucleated and additional growth from that seed is then observed. An alternative representation of the heterogeneous deformation field is furnished by the progressive strain distribution density as a function of the average strain, which is shown in Fig. 16. The strain was evaluated based on the measured displacement field and the strain distribution density $\mathscr{D}(\epsilon)$ was computed by the following expression

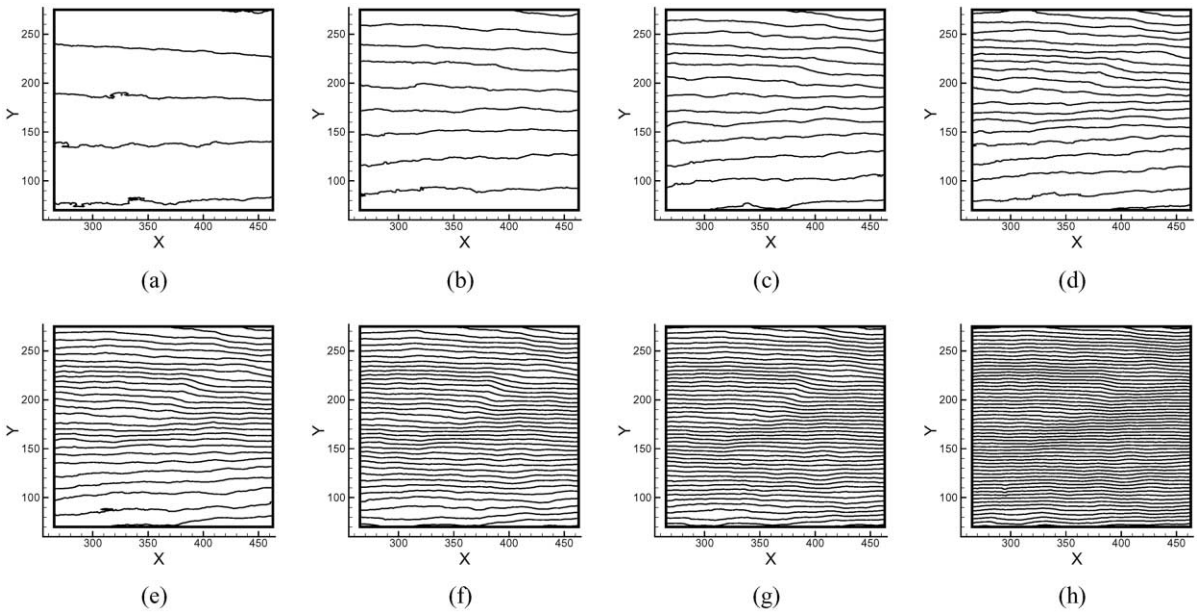

Fig. 15. Progressive deformation field of low density foam based on accumulative displacement contour plot. Lines are contours of equal displacements with increment of 2.5 pixels.

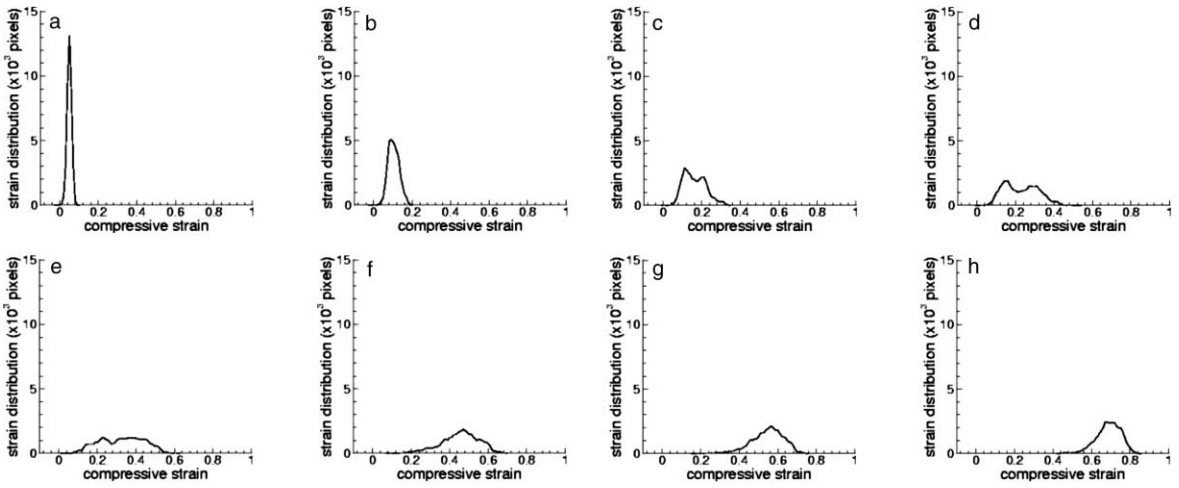

Fig. 16. Strain histograms of low density foam corresponding to progressive deformation.

$$\mathscr{D}(\epsilon) = \frac{1}{MW} \sum_{i=1}^{NW} \delta(\epsilon - \epsilon_i) \tag{25}$$

where δ is the Kronecker delta function, NW is the number of correlation windows used and ϵ_i is the measured strain at the correlation window i. The evolution of the strain distribution density exhibits an initial unimodal distribution, followed by a bimodal and then back to a unimodal, in close general

agreement with theoretical description of a heterogeneous material with imperfect boundary conditions and a finite-width transition layer as depicted in Fig. 13b.

For the heavy foams, with density higher than the critical value ρ_c, the plateau region tends to disappear and the deformation is nearly homogeneous across the sample as shown in Figs. 17 and 18. These observations are also predicted by the theory that postulates that heavy foams exhibit a convex potential

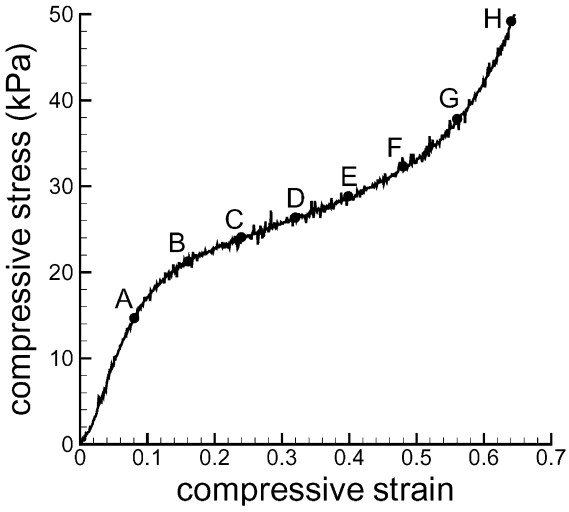

Fig. 17. Stress–strain curve of high density (72 kg/m^3)open-cell polyurethane foam sample under uniaxial compression.

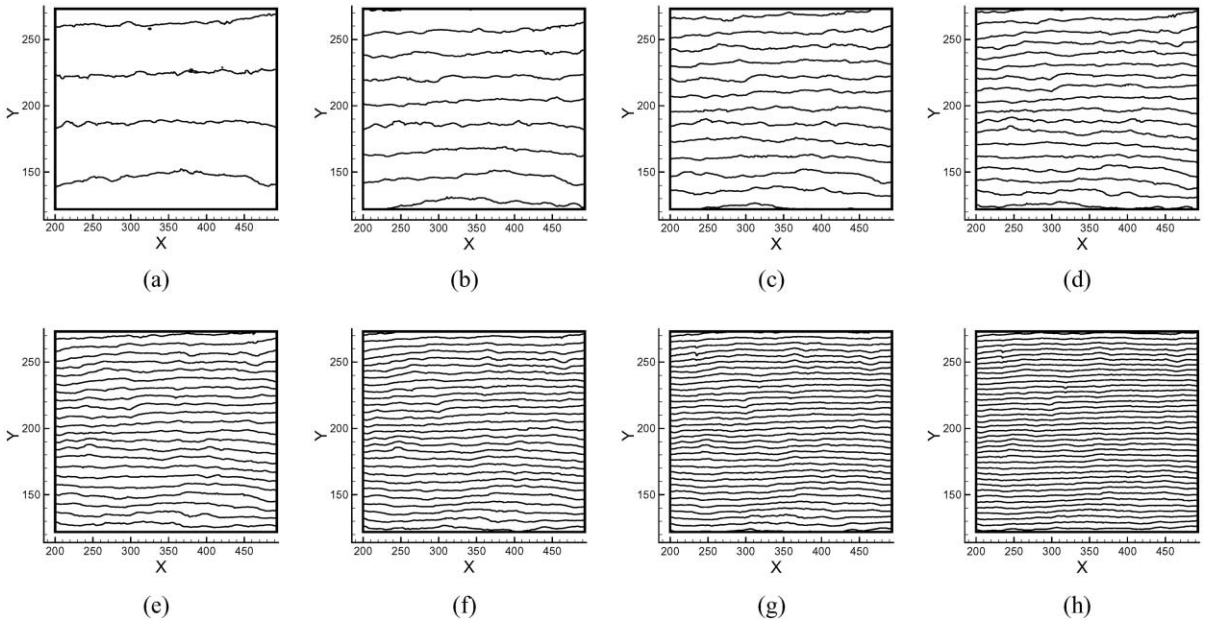

Fig. 18. Progressive deformation field for high density foam based on accumulative displacement contour plot. Lines are contours of equal displacements with increment of 2.5 pixels.

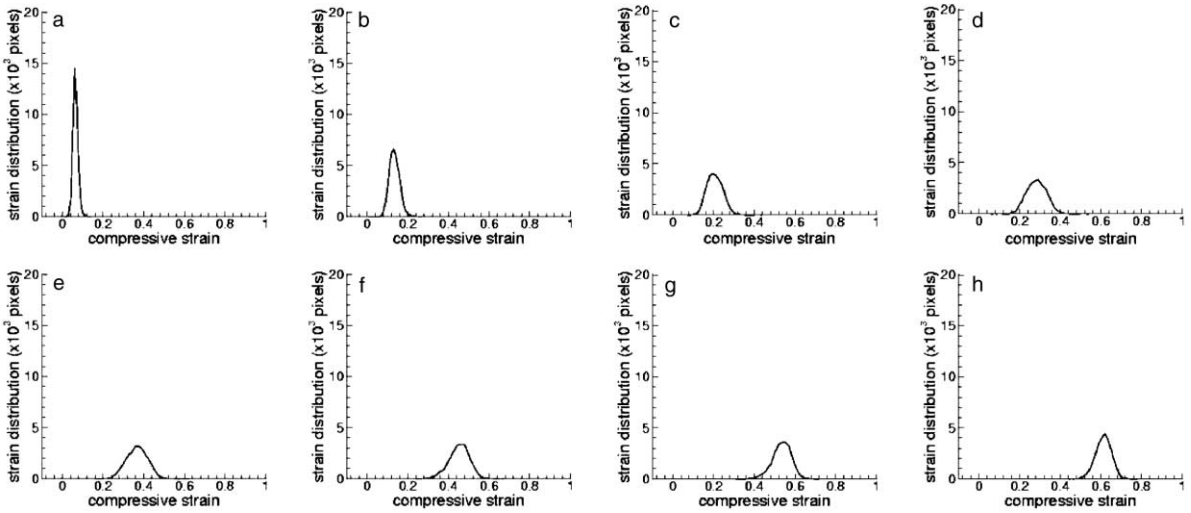

Fig. 19. Strain histograms of high density foam corresponding to progressive deformation.

energy landscape, and therefore, the deformation fields are homogeneous. The specimen tested in this case was a cubic sample of $50 \times 50 \times 50$ mm^3 compressed at a rate of 0.2 mm/s until a strain of $\sim$70% was reached. Fig. 17 shows the stress–strain curve, where the stress is monotonically increasing without the appearance of a stress plateau. In the same plot, the letters *A–H* denote different states along the loading path. For these states, the contour plots of the vertical displacement on the surface of the specimen are shown in Fig. 18. The homogeneous nature of the deformation field is revealed by the equal spacing between the lines at each frame along the loading path. A more conclusive evidence that there is no localization of deformation for this foam is given by the progressive strain distribution density histograms presented in Fig. 19. These plots show that distribution remains unimodal since the inception of the loading until the end.

4. Conclusions

In this article, we introduce a DIC formulation which utilizes a two-step searching algorithm. The first is a coarse search which provides estimates of the displacement field by integer increments of the distance between pixels. During this search the gradient terms are kept constant. The search proceeds by selecting a window in the deform state that best matches one in the reference state. The search is conducted by shifting the window in the deformed state until the merit function reaches a minimum. These estimates are used as initial conditions for the fine search scheme, which is based on Newton–Raphson approach. During the fine search the gradient terms are optimized in conjunction with the displacement field. Displacement continuity across correlation windows is also utilized to improve the computational efficiency of the correlation process. The coarse/fine correlation procedure is local and well-suited for parallelization. An implementation using MPI is also developed.

The formulation is used to study the mechanical behavior of polymeric foams. First the procedure is verified against a set of rigid body motion tests: translation and rotation. These tests show that the correlation procedure is robust and that the natural surface of the foam provides sufficient contrast to compute reliable correlations. It is also shown that the accuracy and precision of the technique is improved by

utilizing a bi-cubic scheme to interpolate the gray level distribution. In addition, an optimal correlation size of 15×15 pixels is found.

The technique is finally used to measure the deformation pattern of relatively light and heavy foams under uniaxial compression. The light foam sample shows a heterogeneous deformation pattern for part of the loading history. This effect is well documented by the histograms of local deformation against average deformation. The measured evolution of the deformation field is consistent with the view that the deformation process occurs as a phase transition. The heavy foam sample shows no localization of the deformation at any stage of the deformation process. This observation is also in agreement with recent theoretical models (Wang and Cuitiño, 2000; Gioia et al., 2001) which predict convex energy densities, and therefore, no phase transition.

Acknowledgements

The support from CAFT at Rutgers University is gratefully acknowledged.

References

Bart-Smith, H., Bastawros, A.F., Mumm, D.R., Evans, A.G., Sypeck, D.J., Wadley, H.N.G., 1998. Compressive deformation and yielding mechanisms in cellular Al alloys determined using X-ray tomography and surface strain mapping. Acta Mater. 46, 3583–3592.

Bastawros, A.F., Bart-Smith, H., Evans, A.G., 2000. Experimental analysis of deformation mechanisms in a closed-cell aluminum alloy foam. J. Mech. Phys. Solids 48, 301–322.

Bay, B.K., Smith, T.S., Fyhrie, D.P., Saad, M., 1999. Digital volume correlation: three-dimensional strain mapping using X-ray tomography. Exp. Mech. 39, 217–226.

Bliss, G.A., 1961. Lectures on the calculus of variations. The University of Chicago Press, Chicago.

Bruck, H.A., McNeill, S.R., Sutton, M.A., Peters, W.H., 1989. Digital image correlation using Newton–Raphson method of partial differential correction. Exp. Mech. 29, 261–267.

Cardenas-Garcia, J.F., Yao, H., Zheng, S., Zartman, R.E., 1998. Digital image correlation procedure to characterize soil surface layer cracking. Agronomy J. 90, 438–441.

Chao, Y.J., Luo, P.F., Kalthoff, J.F., 1998. An experimental study of the deformation fields around a propagating crack tip. Exp. Mech. 38, 79–85.

Chu, T.C., Ranson, W.F., Sutton, M.A., Peters, W.H., 1985. Applications of digital-image-correlation techniques to experimental mechanics. Exp. Mech. 25, 232–244.

Gioia, G., Wang, Y., Cuitiño, A.M., 2001. The Energetics of heterogeneous deformation in open-cell solid foams. Proc. Roy. Soc. London A 457, 1079–1096.

He, Z.H., Sutton, M.A., Ranson, W.F., Peters, W.H., 1984. Two-dimensional fluid-velocity measurements by use of digital-speckle correlation techniques. Exp. Mech. 24, 117–121.

Lockwood, W.D., Reynolds, A.P., 1999. Use and verification of digital image correlation for automated 3-D surface characterization in the scanning electron microscope. Mater. Characterization 42, 123–134.

Lu, H., 1998. Applications of digital speckle correlation to microscopic strain measurement and materials' property characterization. J. Electronic Packaging 120, 275–279.

Lu, H., Cary, P.D., 2000. Deformation measurements by digital image correlation: implementation of a second-order displacement gradient. Exp. Mech. 40, 393–400.

Mizuno, Y., Kawasaki, A., Watanabe, R., 1995. In situ measurement of sintering shrinkage in powder compacts by digital image correlation method. Powder Metallurgy 38, 191–195.

Peters, W.H., Ranson, W.F., 1982. Digital imaging techniques in experimental stress analysis. Opt. Eng. 21, 427–431.

Press, W.H., Teukolsky, S.A., Vetterling, W.T., Flannery, B.P., 1992. Numerical Recipes in C: The Art of Scientific Computing, second ed., Chapter 15: Modeling of Data, Cambridge University Press, pp. 656–706.

Tong, W., 1997. Detection of plastic deformation patterns in a binary aluminum alloy. Exp. Mech. 37, 452–459.

Vendroux, G., Knauss, W.G., 1998. Submicron deformation field measurements: Part 2. improved digital image correlation. Exp. Mech. 38, 86–92.

Wang, Y., Cuitiño, A.M., 2000. Three-dimensional nonlinear open-cell foams with large deformations. J. Mech. Phys. Solids 48, 961–988.

Wissuchek, D.J., Mackin, T.J., DeGraef, M., Lucas, G.E., Evans, A.G., 1996. A simple method for measuring surface strains around cracks. Exp. Mech. 36, 173–179.

Yongqi, S., Corletto, C., Bradley, W.L., Tian, J., 1996. Direct measurement of microscopic strain distribution near a crack tip. Exp. Mech. 36, 193–198.

Zhang, D., Zhang, X., Cheng, G., 1999. Compression strain measurement by digital speckle correlation. Exp. Mech. 39, 62–65.